MDPI

# Experimental and Calphad Methods for Evaluating Residual Stresses and Solid-State Shrinkage after Solidification

Atte Antikainen *[iD], Joni Reijonen [iD], Juha Lagerbom, Matti Lindroos [iD], Tatu Pinomaa [iD] and Tomi Lindroos

Additive and Smart Manufacturing Group, VTT Technical Research Centre of Finland, P.O. Box 1300, 33101 Tampere, Finland
* Correspondence: atte.antikainen@vtt.fi

**Abstract:** Laser powder bed fusion is an additive manufacturing method that is based on melting and solidification of powder material. Due to the local heating above the melting point, thermal stresses are usually formed in the final part. Mitigation of residual stresses is usually assessed by laser scan strategies and not by alloy tailoring. In this paper a segregation-based residual stress formation mechanism is proposed and assessed computationally. Additionally, an experimental setup for rapid screening of residual stress formation in various alloys is proposed. The results should ease material development of metal alloys tailored for additive manufacturing by allowing the comparison of residual stress formation tendency (e.g., solid state shrinkage) between alloys. The proposed computational method is comparative in nature and forecasting absolute residual stress values would require known temperature dependent elastoplastic properties for the alloys as well as exact thermal history. The proposed experimental method is quantitative but its reliability depends on material properties such as yield strength.

**Keywords:** additive manufacturing; segregation; thermal expansion; residual stress

## 1. Introduction

Laser powder bed fusion (LPBF) is a widely used additive manufacturing (AM) method for complex, lightweight high technology applications and the commercially available materials cover a variety of alloy groups such as iron, nickel, titanium, aluminum and copper based alloys [1]. Many of the available alloys possess high strength, which in combination with selective melting and solidification, can lead to very high residual stress formation. Residual stresses can cause the manufactured part to fail by cracking or warping, or even failing to build at all. The issue can, to some extent, be avoided with sufficient support generation and stress relieving heat treatment [2]. However, in some cases even solid supports cannot restrict the piece from cracking and warping. In such case, the material is too weak to withstand the stresses it generates during solidification [3]. Once the piece has been cracked, heat treatments are usually not sufficient to recover the manufactured piece. Furthermore, residual stresses can have a large negative effect on properties such as fatigue and corrosion resistance [4]. Therefore, controlling residual stresses is paramount in order to manufacture operational components [3,5].

Modeling of AM is a multi-physical problem that utilizes computational tools such as Calphad, phase field, finite element method, micromechanics and crystal plasticity [3,6–8]. In many cases, different features of AM process have been studied separately. Ahmed et al., have studied the effect of material properties on calculated melt pool temperature by using finite element method (FEM) to simulate moving heat source on a surface [9]. The non-uniform heating causes material-dependent thermal stresses that can be calculated from the solved temperature field. For example, Fergani et al., studied analytically the thermal stress formation in 316L during LPBF [10]. The forming grain structures can be investigated more thoroughly with phase field simulations [11–13]. Crystal plasticity

and phase field simulations have been succesfully utilized in evaluating residual stress formation in additively manufactured 316L by considering solidification- and dislocation structures [14–16]. The simulation part of this work focuses on the Calphad method. Calphad utilizes pre-determined and experimentally validated databases to calculate properties, such as the molar volume, of multicomponent systems [17].

An established experimental method to assess the effect of process parameters, scan strategy or chemical composition has been the manufacturing of cantilever samples, which has also been used to validate thermomechanical simulations [18–20]. Other geometries such as bridges [21], L-shaped or prisms [22], or warping of entire build platform [23] have been used for the same purpose. Wu et al., studied the residual stress formation in LPBF 316L with neutron diffraction and digital image correlation, showing that residual stresses depend on scan strategy, location and direction [22].

In addition to scan parameters, global printing parameters such as platform pre-heat temperature and waiting time have been applied in aspiration for controlling residual stresses. Denlinger et al., studied the effect of interlayer dwell time on residual stress formation in Ti64 and In625 alloys during direct energy deposition (DED) process. For Ti64 nonexistent dwell time minimized the residual stresses, whereas for In625 the residual stresses decreased when additional cooling time was provided [24], which shows the importance of taking chemical composition into account when developing measures for residual stress control. Mertens et al., studied the influence of build platform preheating on residual stresses in H13 tool steel and found stresses changing from compressive into tensile stress when pre-heat temperature was increased from no pre-heating to 400 °C [25]. Buchbinder et al. [20] reported significant reduction in AlSi10Mg cantilever displacement when build platform preheat temperature was increased.

Comparison of residual stress formation between alloys is difficult, because process parameters and location in the sample have a large effect on the residual stress values. Moreover, the concept of residual stress is not unambiguous, but it can be categorized into three groups. Type I residual stresses influence over several grains and may cause macroscopic distortion. Type II is considered intergranular and type III as interatomic stresses [26,27]. A good summary of residual stress values in some alloys can be found in a review article by Bartlett and Li [27]. Their survey shows Ti64 generating higher maximum stresses (600 MPa) than 316L or commercially pure titanium (250 MPa) and maximum residual stress being inversely proportional to thermal diffusivity of the material. However, thermal diffusivity does not take elastoplastic behavior into account and it assumes the material is homogeneous, which in the case of solidification of alloys, is not true in the microstructural level.

To the authors knowledge, none of the existing research done in the area covers the effect of chemical inhomogeneity on thermal expansion of the material, even though Fergani et al. [10] have recognized the issue. In this work, the effect of segregation on thermal expansion and hence on type II/III residual stresses is investigated with Calphad method. The simulations are complemented with an experimental method which can be used to determine type I residual stresses on laser surface melted samples. This work aims to ease material development for solidification-based manufacturing processes such as LPBF or DED, by presenting means to calculate the solid-state shrinkage considering segregation.

## 2. Materials and Methods

An experimental method for evaluating residual stresses during laser processing was developed. The idea is based on work by Stoney [28] and Brenner and Senderoff [29] which is further elaborated in a book by Ohring [30]. Here the evaluation of materials' tendency to form residual stresses relies on sufficiently thin samples that are lasered on one side. Surface melting and solidification can cause a measurable curvature of the sample, from which the stress in melted area can be derived, when elastic properties of the material are known. This approach has been applied for example in cold sprayed coatings [31] and directed energy deposition [18,19,24]. The curving of such samples is nicely illustrated by Simson

et al., who studied residual stresses in laser powder bed fusion [32]. Here laser has been used without powder because the intention is to speed up material development process and hence to avoid atomizing and testing with powders as much as possible. Instead, the sample materials can be alloyed, cast and cut into solid samples for analysing the effect of composition on the behaviour under laser melting. The laser melted surface has to be sufficiently thin in order to reduce the error when using analytical equations to calculate the stresses, but thick enough to cause measurable curvature. Too high melt depth to sample thickness ratio can lead to plastic deformation of the sample, resulting in unnaturally high residual stress values, because Equation (2) that is used to calculate the stress assumes elasticity only. Thickness of the melt layer and the substrate have to be measured, which in this case were measured from images taken with ZEISS (Jena, Germany) Axio Observer Inverted Microscope. Because the melt pool bottom is curved, the average thickness of the melt surface was measured from areas as shown in Figure 1 The surface was etched to highlight the melt area from the surface. The chord (*B*) and sagitta (*Z*) of the curved samples were measured with ImageJ software (version 1.53b, National Institutes of Health, Bethesda, MD, USA) as illustrated in Figure 2. The curvature (inverse of radius *r*) of the sample was then calculated from Equation (1) by using the measured values for *B* and *Z* [29]. Curvature and required material properties such as Poisson's ratio and elastic moduli of the substrate and the lasered area are used to calculate the residual stress values in the lasered area with Equation (2), where $\sigma_f$ is the stress in melt material, *Y* Young's modulus, *d* thickness, *v* Poisson's ratio, and *R* curvature. Subscripts *f* and *s* represent lasered and base material respectively [30].

$$\frac{1}{r} = \frac{2Z}{B^2 + Z^2} \tag{1}$$

$$\sigma_f = \frac{1}{d_f(d_f + d_s)}\left(\frac{Y_f d_f^3}{6R(1 - v_f)} + \frac{Y_s d_s^3}{6R(1 - v_s)}\right) \tag{2}$$
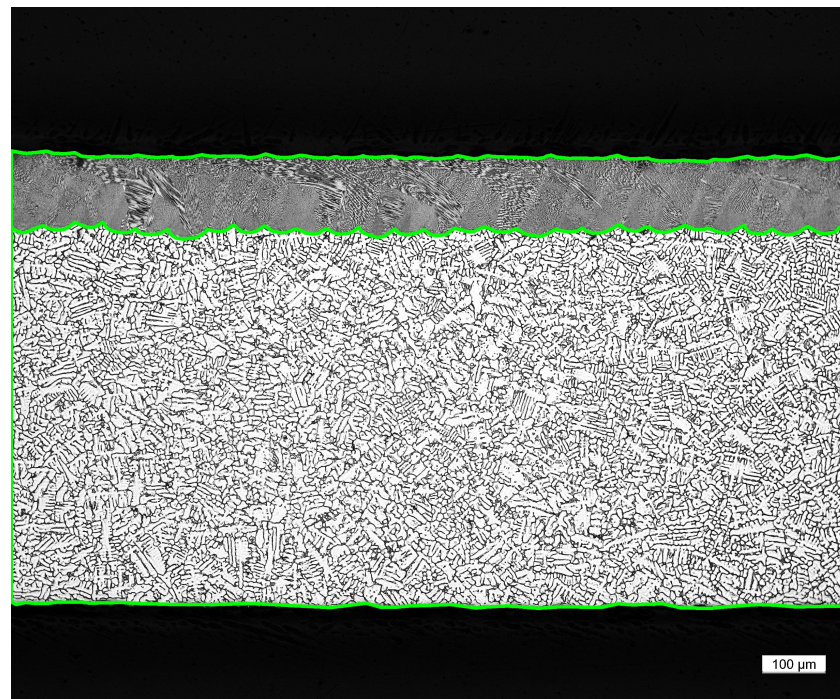


**Figure 1.** Measured areas from which the average thickness of the sample and the melt were calculated.
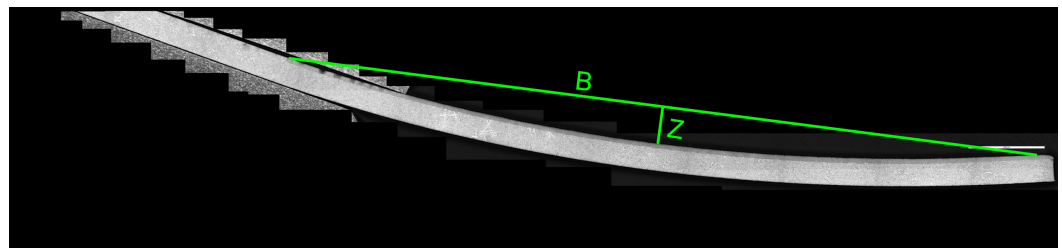
**Figure 2.** Curvature measurement by chord-and-sagitta-method.

Investigated compositions were stainless steel 316L, cold work tool steel D2, Inconel HX, Ti64 and commercially pure (TiCp) grade 2 titanium. Five samples of 316L, D2 and TiCp, four of Inconel Hx and two of Ti64 were used for this study. 316L and Titanium grades were supplied as cold rolled sheet with a nominal thickness of 0.8 mm. Inconel HX was supplied as 0.9 mm thick sheet. D2 was induction vacuum melted, copper mold cast and sliced to nominal thickness of 0.7 mm in-house. Materials were cut into residual stress specimens of approximate dimensions of 25 × 10 mm. Cold rolled sheets were stress relieved for 2 h at 800 °C in vacuum atmosphere to ensure low initial stress state, whereas D2 was lasered in as cast condition. The top surfaces of the samples were slightly ground before lasering to normalise the surface. The lasering was done with a SLM125HL (SLM Solutions, Lubeck, Germany) laser powder bed system with 1070 nm wavelength and 80 µm spot size at focus. Scan parameters were power of 175 W, scan speed of 720 mm/s and a hatch distance of 50 µm. A 600 ms delay was added after each laser vector to avoid excess heating and in-situ stress relieving of the thin sample. Scanning begun from the free-hanging tip of the sample and scan vector direction was perpendicular to the longest edge. The scanning was done in an inert argon atmosphere. The experimental test setup and scanned Ti64 samples are shown in Figure 3. For comparison, scanned 316L are shown in Figure 4 before and after scanning.
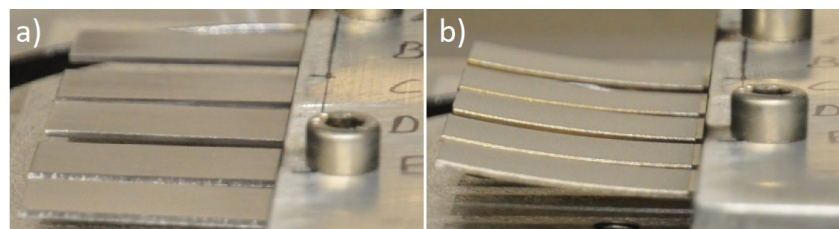


**Figure 3.** Test setup and Ti64 samples (**a**) before and (**b**) after laser scanning.
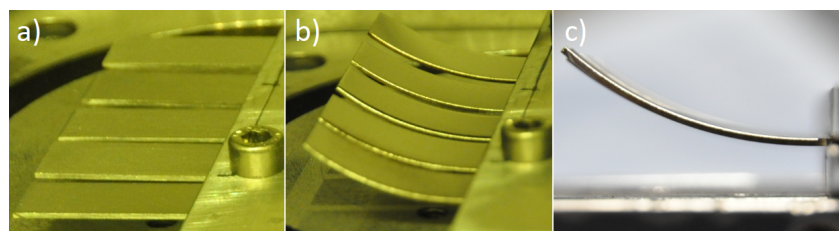


**Figure 4.** 316L samples (**a**) before and (**b**,**c**) after lasering.

The computational analysis of residual stress tendency was simulated with Thermo-calc 2021a (Thermo-Calc Software AB, Stockholm, Sweden), TCFE11 database and TC-Python interface. In the TC-Python interface, a standard Scheil simulation was calculated first. The Scheil result was used to calculate composition of each solidified layer by subtracting the elements consumed from the liquid between each temperature step. Once the composition of each layer was acquired, the compositions were fed into a loop of property diagram calculations. The phases were allowed to form freely in the Scheil module, but the phases chosen in the property module were determined based on literature and XRD measurements of rapidly solidified samples. Liquid+FCC system was used for

316L [33] and Inconel HX [34] whereas Liquid+FCC+M7C3 was used for D2 [35]. Two systems were calculated for titanium alloys consisting of Liquid+HCP or liquid+HCP+BCC phases [1]. From the property diagram calculations, temperature-dependent molar volume ($V_m$) was extracted and used to calculate the linear coefficient of thermal expansion (CTE, $\alpha$) according to Eequation (3) as presented by Lu et al. [36]. In this study, due to the variation in investigated material groups, the magnetic term in the original equation has been neglected. As a result, temperature-dependent CTE as a function of solidified layer, e.g., segregation, is acquired.

$$V_m(T) = V_0 exp\left(\int_{T_0}^{T} 3\alpha dT\right) \tag{3}$$

Here an assumption is made that the density of solid is constant (mass fraction $m_f$ is used as volume fraction) and that the solidification takes place in dendritical or cellular manner, where the forming features or sub-features are cylindrical. With these assumptions, mass fraction of solid is used as a relative thickness of the solidified layer $L$ on a cylindrical surface. Each layers' distance from the dendrite center was calculated from Equation (4) as indicated by $r_{layer}$. If the solidification was considered planar, Equation (4) would not be required and mass or volume fraction of the solid could be used directly as a distance from the meltpool wall. Equiaxed solidification could be approximated by assuming spherical crystals and the equation for $r$ in such case would be formulated from the volume of a sphere. For all solidification modes, the solidified layer thicknesses $L_n$ are calculated by subtraction $L_n = r_n - r_{n-1}$.

The simplified solidification structure is shown in Figure 5 where $L_n$ represents the thickness or mass fraction of the solidified layer and $\alpha_n$ is the corresponding linear thermal expansion coefficient. The length change per temperature unit was calculated for each solidified layer $L_n$ by using the previously calculated $\alpha_n$ and Equation (5) which is the simple equation for thermal expansion. Since $\alpha$ is calculated as a function of solidified layer, Equation (5) can be summed over the entire solid, resulting in total length change per temperature unit $P_{tensile}$ as shown in Equation (6) where the subscript n indicates the number of the solidified layer.

$$r_{layer} = \sqrt{m_{fsolid}/\pi} \tag{4}$$

$$dL_n = \alpha_n L_n dT \tag{5}$$

$$P_{tensile}(T) = \sum \alpha_n(T) L_n \tag{6}$$

Because $L$ is a fraction without unit, Equation (6) gives the mean thermal expansion for the segregated system at a certain temperature. For analyzing shrinkage over the entire cooling range, $P_{tensile}$ can be integrated over a chosen temperature range according to Equation (7). In this research, low temperature limit was set to 400 °C.

$$S = \int_{T_{min}}^{T_s} P_{tensile} dT \tag{7}$$

The integration results in a single dimensionless number $S$ that is the total shrinkage of the segregated system. The total shrinkage can be used to calculate average CTE for the system when the cooling range is known. Average CTE for 316L was used in Comsol 6.0 to evaluate the role of plasticity in the results, which is presented in the Appendix A.
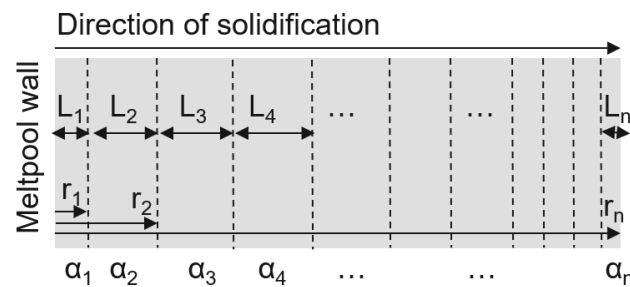
**Figure 5.** Schematic representation of the simplified solidification.

## 3. Results

Calculated temperature and segregation dependent thermal expansion data were imported to Comsol 6.0 (COMSOL AB, Stockholm, Sweden) as grid-type data for plotting. The thermal expansion coefficient versus distance from dendrite/cell center and temperature plots for 316L, D2, Ti64 (HCP+BCC system) and Inconel HX are shown in Figure 6.
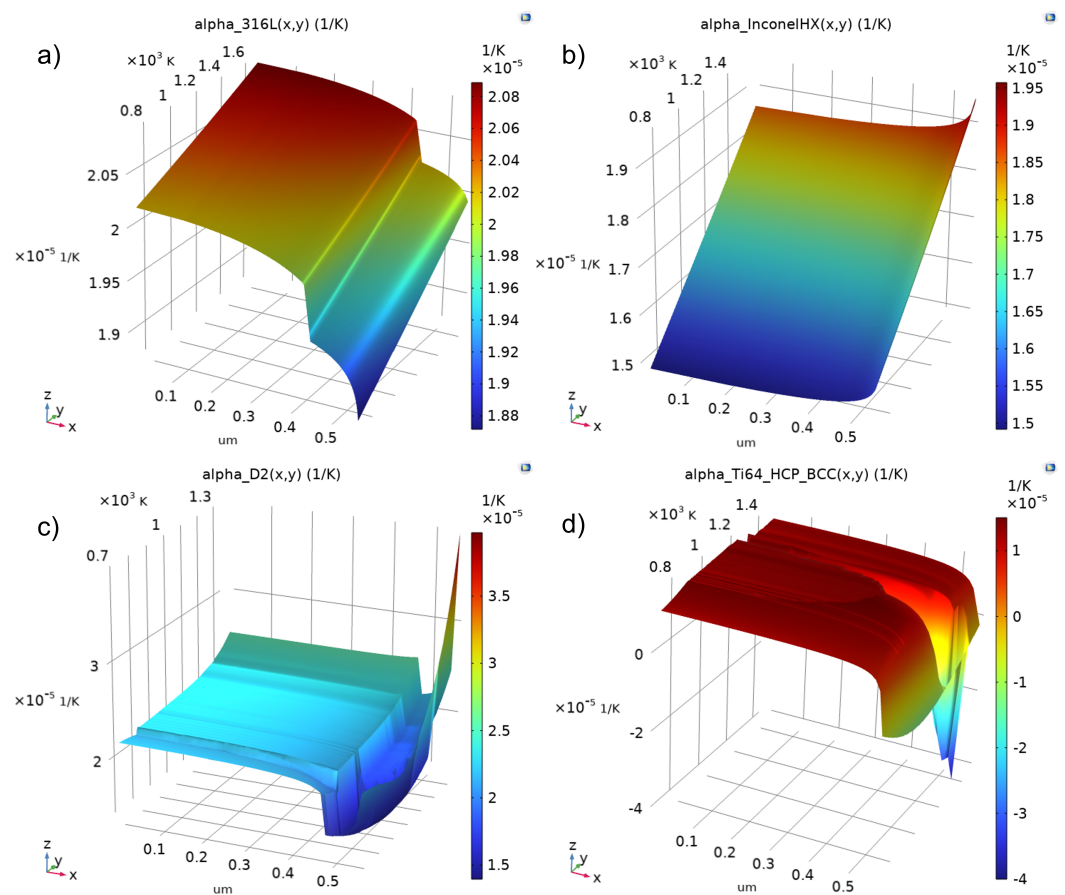


**Figure 6.** Segregation and temperature dependent thermal expansion coefficients for (**a**) 316L, (**b**) Inconel HX, (**c**) D2, (**d**) Ti64. Distance *r* from dendrite core is shown on x-axis, temperature on y-axis and CTE on z-axis.

Figure 6 shows the CTE (z-axis) of investigated materials with respect to distance from dendrite core (x-axis) and temperature (y-axis). From the investigated materials 316L and Inconel HX show the smoothest isosurface plots because of their single phase FCC structure in the property diagram calculations. However, 316L (Figure 6a) solidifies first as BCC which is followed by nucleation of FCC, whereas Inconel HX (Figure 6b) solidifies as FCC. This difference in solidification causes a step in CTE of 316L, even though the solid-state CTE's are calculated for a fully austenitic FCC system. Phase transitions in D2

and Ti64(HCP+BCC) generate valleys and high or low spikes depending on the volume change of the transition. In Figure 6c segregation-based M7C3 carbide formation is the most likely cause to the peak at dendrite boundary. Such high values could exist because of melting, but the melting point of grain boundary phase in segregated D2 was checked with Thermo-calc and even for that composition solidus is not exceeded in Figure 6c. Similar phenomena is seen in the TiCp(HCP)-calculation in Figure 7, but there the system begins to melt at 1702K when high temperature BCC phase is not allowed to form. For this reason, HCP+BCC system is considered as more feasible system for the titaniums. This issue is further illustrated in Appendix B.
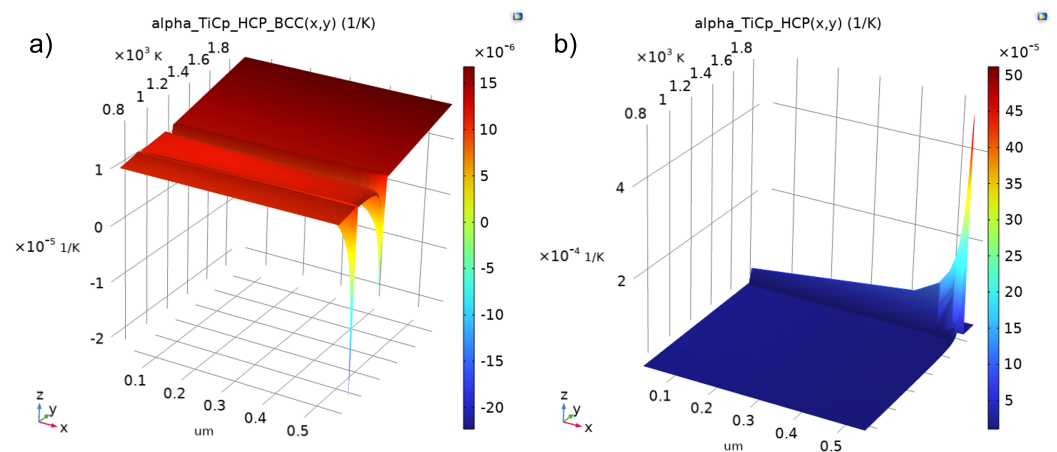


**Figure 7.** Calculated CTE for (**a**) TiCp(HCP+BCC) and (**b**) TiCp(HCP). Distance *r* from dendrite core is shown on x-axis, temperature on y-axis and CTE on z-axis.

From the figures it is evident that thermal expansion coefficient is a function of composition (segregation) and temperature. The distance from dendrite center is scaled such that volume fraction of the entire dendrite is 0.99 because of the Scheil simulation stop condition at 1% liquid. Here volume fraction is the same as area fraction, and therefore *r* for area fraction unity can be calculated from $A = \pi r^2$ which results in a dendrite radius of approximately 0.561 μm, depending on the exact stopping of the Scheil calculator. The radius can be scaled to correspond measured data from micrographs, but since rapid cooling can result in very small dendrite arms in this article the 0.561 μm radius to plot the CTE data are used as-is.

The results from Thermo-calc simulations are shown in Table 1. Solidus temperatures are tabulated for each Scheil–Gulliver simulation. Average CTE and linear shrinkage is calculated from solidus minus 50 K to 673 K. Table 1 shows D2 steel having the largest average CTE between the temperature limits. The exceptionally high CTE value for D2 when compared to literature values originates from the fully austenitic metastable microstructure that was confirmed with XRD measurements [35]. The CTE of rapidly solidified sample was verified with dilatometry ($21 \times 10^{-6}$ 1/K, 150–500 °C) and it was in very good agreement with the simulated result. Once the sample had been annealed during the first measurement cycle, the CTE of rapidly solified D2 was lowered to $14 \times 10^{-6}$ 1/K as seen in Figure 8. 316L has slightly lower CTE than D2, but still larger than Inconel HX.
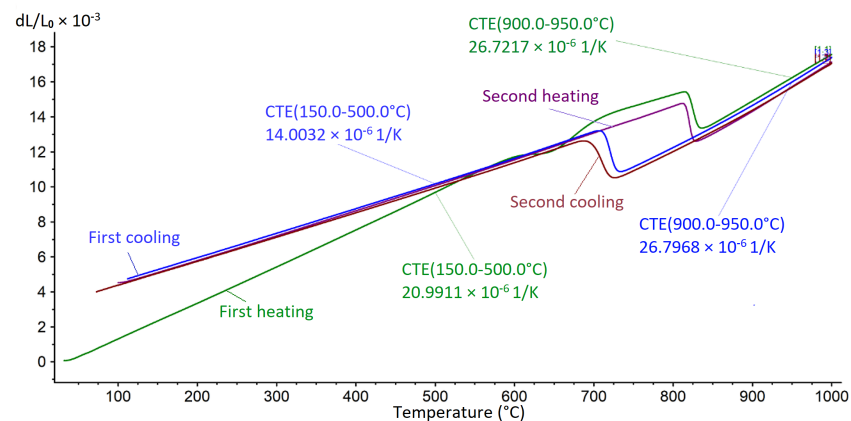
**Figure 8.** Dilatometry curve for rapidly solidified D2 steel.

The total shrinkage of each investigated material are shown in Figure 9. Shrinkage was calculated from 1373 K to 673 K in increments of 50 K. If hot strength of the material can be estimated to some extent, Figure 9 can be used to evaluate the shrinkage that causes stress accumulation by assuming zero-stress temperature above which stresses are negligible. Both steels have similar shrinkage, even though in D2 the austenite is mainly stabilized by carbon and M7C3 carbides are allowed to form, whereas 316L is fully austenitic and stabilized by nickel. Based on Figure 9, most shrinkage should occur in D2 when cooled from 1373 K.

Two titanium systems were calculated to see the effect of BCC-HCP phase transformation taking place during cooling, even though the appearance of low temperature liquid phase in the HCP only system causes some error. The least shrinkage takes place in Ti64, where the expansion of BCC-HCP reaction starting at around 1273 K essentially cancels the effect of thermal shrinkage between 1173–1273 K. Similar but smaller plateau is seen in TiCp HCP+BCC system, where the BCC-HCP plateau begins at lower temperature. Down from approximately 950 K the shrinkage of all Ti-calculations show similar shrinkage.
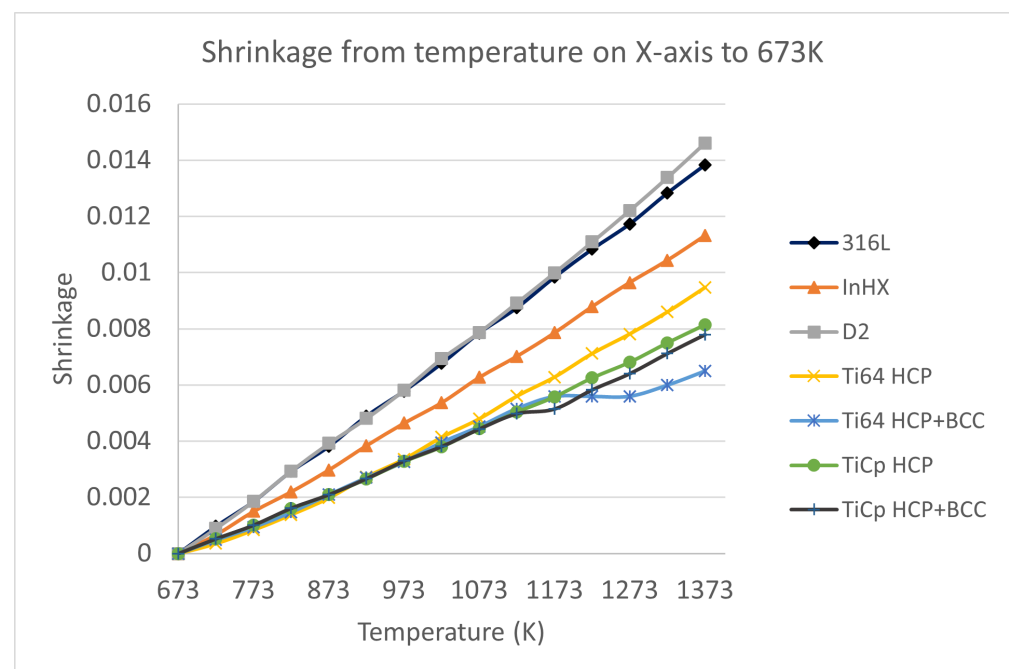


**Figure 9.** Total unrestricted shrinkage from high temperature (on x-axis) to 673 K.

**Table 1.** Calculated solidus temperatures, average thermal expansion coefficient and shrinkage from solidus minus 50 K to 673 K. Titanium values are for the HCP+BCC system.

| Alloy | Scheil Solidus (K) | $\alpha_{ave}$ (1/K) $T_{(sol-50K)}$-673 K | Linear Shrinkage $T_{(sol-50K)}$-673 K |
|---|---|---|---|
| 316L | 1678 | $19.9 \times 10^{-6}$ | 0.019 |
| D2 | 1397 | $20.8 \times 10^{-6}$ | 0.014 |
| Ti64 | 1499 | $9.48 \times 10^{-6}$ | 0.007 |
| TiCp | 1919 | $12.8 \times 10^{-6}$ | 0.015 |
| In. HX | 1614 | $16.7 \times 10^{-6}$ | 0.015 |

Thicknesses of the measured melt surface layers and base materials are shown in Table 2. All substrates were lasered with the same laser parameters. It is observed that melt thickness of Inconel HX is the smallest and its substrate was the thickest. The steels' 316L and D2 surface thicknesses are comparable at 131 µm and 118 µm, respectively. Error in D2 measurements is outstandingly small due to better edge retention during etching resulting in more evenly focused optical images. Titanium samples show the deepest melts of around 190 µm.

**Table 2.** Measured thicknesses of laser melted surface and the base material. Laser parameters were 175 W power, scan speed of 720 mm/s and a hatch distance of 50 µm. Standard deviation is used as margin of error.

| Alloy | Melt (µm) | Base (µm) | Total (µm) |
|---|---|---|---|
| 316L | $131 \pm 14$ | $673 \pm 5$ | $803 \pm 11$ |
| D2 | $118 \pm 1$ | $592 \pm 3$ | $710 \pm 3$ |
| Ti64 | $184 \pm 7$ | $651 \pm 11$ | $835 \pm 18$ |
| TiCp | $193 \pm 10$ | $629 \pm 13$ | $822 \pm 22$ |
| Inconel Hx | $95 \pm 3$ | $840 \pm 28$ | $935 \pm 28$ |

Residual stresses calculated with Equation (2) and most important mechanical properties related to the experimental method are shown in Table 3. The measured residual stress values are very high for all other than titanium samples. This may be explained by their low yield strength and high elastic modulus. 316L has the lowest yield strength that might be the cause for extreme measured stress values. Even though the yield strength of D2 substrate is much higher than for 316L, high CTE may have caused local plastic deformation. However, regardless of larger CTE of D2 over 316L, D2 shows less residual stress suggesting less plastic deformation. Inconel HX shows also implausible measured stress value, which is assumed to result from plastic deformation of the base material. Ti64 and TiCp show most reasonable residual stress values even though measured residual stress for TiCp still exceeds yield stress of the base material. For Ti64 the measured residual stress value is reasonable as it is much below the assumed yield strength and in agreement with the lower limit of the stress values shown in [27].

**Table 3.** Measured residual stresses. Standard deviation is used as margin of error. Five samples of 316L, D2 and TiCp, four of Inconel Hx and two of Ti64 were measured. * Approximation.

| Alloy | Measured Res. Stress (MPa) | $\sigma_y$ Base (MPa) | $\sigma_y$ LPBF (MPa) | Young's Modulus (GPa) |
|---|---|---|---|---|
| 316L | $3071 \pm 214$ | 170 [1] | 450 [1] | 193 [37] |
| D2 | $2134 \pm 98$ | >700 * | 1203 [38] | 190 [38] |
| Ti64 | $325 \pm 18$ | 880 [39] | 945 [40] | 114 [39] |
| TiCp | $372 \pm 21$ | 362 [41] | 560 [42] | 103 [41] |
| In. HX | $1709 \pm 213$ | 345 [43] | 630 [44] | 205 [43] |

## 4. Discussion

### 4.1. Experimental Method

Simple experimental method for manufacturing samples and calculating residual stress in a surface-lasered sample was presented. The experimental method is based on substrate curvature measurements from which the residual stress value in lasered surface layer is calculated. The analytical Equation (2) uses lasered layer and base material thicknesses and sample curvature as arguments, and assumes all deformation takes place elastically. However, due to large stresses originating from solidification and cooling, the assumption of only elastic deformation may not hold with all materials. Furthermore, rapid solidification usually increases the yield strength of the investigated materials, which can make the weaker base material more prone to plasticity. This is shown clearly in Figure 6 where most of the materials show erroneously high residual stress values exceeding yield strength, which is most likely a result of plastic deformation in the sample. Residual stresses close to [27] or exceeding [34,45] the yield strength of LPBF materials have been reported, which is in accordance with the present observation of plastic yielding. For this reason, the method is considered better suited for high strength materials where plastic deformation is unlikely. Only titanium samples show reasonable measured residual stresses when compared to LPBF yield strength, which makes sense, because their Young's moduli are significantly lower than that of Fe- or Ni- based samples allowing more elasticity with less force. In addition, Figure 9 show Ti-samples having lowest shrinkage of the samples, making them less prone to stress accumulation and plastic deformation. An example of FEM compensation of plasticity in 316L is presented in Appendix A.

Yield point is typically specified as the point where plastic strain is 0.2%. Many heavily alloyed metals, such as D2, show brittle behaviour after rapid cooling, but even in those cases the fracture elongation can be above some percent. Such elongation is very small regarding engineering applications, but for the Equation (2) that relies to the assumption of elastic bending only, one percent of plastic elongation can cause a large error as seen in the results. Sample materials in sheet form were annealed before lasering to relieve existing residual stresses. The purpose was to rule out the effect of existing stresses on the measured residual stresses. However, as it turned out, the error caused by plasticity is considerable and thus using cold worked (i.e., stronger) samples might have given better results regardless of their assumably non-zero initial stress. The plastic deformation can be minimized by thickening the sample, but it will decrease the curvature and make the measurement more prone to error. Because thickness of the solidified layer $d_f$ and the substrate $d_s$ are risen to the third exponent in Equation (2), they should be measured as accurately as possible. However, the base material directly below the melt and solidified layer would still be prone to plastic deformation, which might have been the case for Inconel HX because the melt-to-substrate ratio was the lowest and it still shows unnaturally high residual stress. No cracks were observed in any of the samples. Most sample materials are ductile, but the D2 sample is fairly brittle. Even though cracks would make the stress calculations invalid, they would be visible with optical microscopy and hence be easy to take into account.

### 4.2. Computational Method

A Calphad-based computational method for estimating solid-state shrinkage in a segregated material was developed and presented in this article. The method allows to rapidly screen shrinkage of multiple alloys that are processed via solidification. The results can be used as guidance for developing novel compositions for additive manufacturing. The solidified layer compositions were calculated using Scheil–Gulliver model and the composition of each layer was introduced in separate calculations to calculate the temperature-dependent CTE for each layer. Therefore, the method can be utilized to evaluate metastable behaviour of the system that allows only very short range diffusion (each layer approximated to be in equilibrium with itself) and diffusionless transformations, because the phases can be allowed to form freely in each of the layers, but the composition

of each layer is fixed. However, knowledge of most likely forming phases is very useful in order to create as representative computational system as possible. Even though Ti64 is known to form alpha prime martensite during LPBF, the implementation of this metastable phase in the presented calculation method seemed problematic. For materials without solid state transformations such as Inconel HX and 316L the forced single-phase approximation generated fine results and the effect of segregation on CTE is clearly visible in Figure 6a,b. When more phases are allowed to form, the results become more complex as is seen for D2 and Ti64 in Figure 6c,d, respectively. The most interesting feature of Figure 6c,d is that the most profound change in thermal expansion coefficient takes place at the vicinity of the grain boundary due to segregation, confirming the original hypothesis.

The results clearly show how thermal expansion coefficient varies due to segregation based inhomogeneity. Furthermore, the temperature dependence of each solidified layers' alpha can vary. This knowledge can be used to develop materials for AM with minimized and as uniform shrinkage as possible. High alpha can be mitigated with pre-heating to reduce $dT$, but pre-heating does not mitigate the type II internal stresses caused by non-uniform CTE. $P_{tensile}$ covers only the linear strain of a 1-dimensional system. Therefore another variable for potentially forming shear stresses is suggested to describe the mismatch of thermal expansion coefficients in the layer interface as shown in Equation (8).

$$P_{shear}(T, L) = |\alpha_L(T) - \alpha_{L+1}(T)| \tag{8}$$

$P_{shear}$ is the shear potential that represents the mismatch in thermal expansion coefficient between subsequently solidified layers. For example, a material with a homogeneous $\alpha$ would show zero $P_{shear}$ but only some $P_{tensile}$. The shear stress in each interface would be proportional to $dT$ and depend also on the elastic modulus of the material. More thorough investigation of type II shear stresses is left for further research.

316L and Inconel HX were simulated as fully FCC, so phase transformations are not present and the CTE versus temperature and distance from dendrite core graphs look fine in Figure 6. On the contrary, both Ti-samples show the effect of BCC-HCP phase transformation on shrinkage in simulations where the transformation is allowed in Figures 6d and 7a. Due to the transformation, the Ti HCP+BCC shrinkage curves in Figure 9 have a plateau that cancels the effect of cooling shrinkage. The location and length of the plateau depends on the alloying element content and segregation, which are larger in Ti64 than in TiCp. If we consider Ti64 in Figure 9, shrinkage would be constant when cooling from a temperature range between approximately 1173–1273 K due to BCC-HCP transformation. To minimize the forming stresses, the temperature range of this constant-volume cooling can be adjusted by alloying to take place below recrystallization temperature to minimize residual stresses. The plateau in Figure 9 is seen in Figure 6e as negative thermal expansion coefficients due to expansive volume change between BCC-HCP transformation during cooling. By comparing the titanium data between HCP and HCP+BCC systems it is be presumed that BCC-HCP transformation during cooling would reduce residual stresses by reducing shrinkage.

The selection of solidification mode is important for the coupling between mass fraction solid given by the Scheil–Gulliver simulation and the layer thickness. It is obvious from Figure 10 that in other modes than planar, certain fraction of solid results in differently thick layers based on the $r$ at the time of solidification. In other words, the first composition to solidify will form larger $L$ compared to if the same mass fraction was solidified last. Equation (4) is used to convert the mass fraction from Scheil–Gulliver simulation into an axisymmetric situation of layer thicknesses.
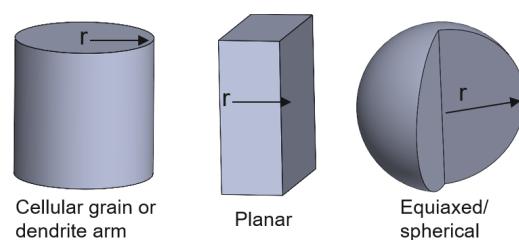
**Figure 10.** Schematic representation of simplified modes and respective *r*.

In this paper only dendritic and cellular solidification are considered when calculating the *r* for each layer, because they both consist of features that can be approximated as cylindrical and Inconel HX [46], 316L [47] and D2 (Appendix C) are known show such microstructures. Microstructures of LPBF Ti64 and TiCp consists of fine laths [1] for which the dendritic approximation is not be the best. The main difference between cellular and dendritical evaluation is in determining the radius of the segregated unit, which in this study was 0.561 μm, which is a reasonable value for fine secondary dendrite spacing as illustrated in Appendix C. For cellular 316L the value could be slightly larger at around one micron as shown in [47]. The exact dimensions depend on cooling rate so universal values cannot be given. Size and shape of rapidly solidified grains can be easily obtained by characterization of single track laser scans of solid samples [48].

As Equation (5) shows, the length change is relative to thermal expansion coefficient and change in temperature. The investigated materials have different alphas, but also different solidus temperatures. In Table 1 we see 316L having the highest linear shrinkage between solidus minus 50 K and 673 K. If the formation of thermal stresses was evaluated solely on (5), high solidus would cause high stresses because of the *dT* term. In practice this is not true, because materials deform plastically at elevated temperatures. Therefore, it is likely that materials with good high temperature mechanical properties in as-manufactured state may cause cold cracking issues due to high *dT* during which stresses can accumulate. To truly simulate the solid state stress formation, temperature-dependent stress-strain data would be required all the way from solidus to lower temperature, and usually such data are not available for novel materials at the initial stages of material development. The role of high temperature plasticity is assessed briefly in Appendix A.

*4.3. Future Work*

Future work will focus on making the proposed methods more robust. At the current state the computational method works best for single phased alloys because the non-equilibrium phase proportions for multiphase systems are difficult to include properly. The boundary conditions and settings for Scheil–Gulliver simulation will be investigated in the future with varying cooling rates (back-diffusion) and solute trapping to see how they affect thermal expansion behavior. Similarly, the conditions for subsequent property model simulations will be investigated more thoroughly to allow better representation of the metastable phase proportions during phase transformations and carbide formation. For some of the tested compositions, carbide formation caused poor convergence which should also be improved. Now the phase selection for all property diagram calculations is the same, but this will be made adaptive to allow more detailed phase structures to be simulated. Thorough experimental characterization is required for validation, which can be very laborious, and hence it was not possible to be included in this work.

**5. Conclusions**

A Calphad-based computational method for calculating solid state shrinkage after solidification was presented. The results show segregation generating non-homogeneous thermal expansion coefficients within the material. The presented method can help scientists and material engineers to develop alloys for additive manufacturing and other processes that contain solidification and subsequent cooling. Furthermore, an experimental

method for evaluating materials tendency to form residual stresses during laser melting was introduced. The experimental method can provide quantitative residual stress values for surface-lasered materials if the base material does not yield plastically. Therefore, the method is considered most suitable for high strength materials where plastic yielding is at minimum. If mechanical property data are available or can be approximated for the investigated material, the plasticity can be compensated with FEM simulations.

Advantages:

- No additive manufacturing required for residual stress analysis (Exp.)
- Simple measurement from optical microscopy images (Exp.)
- Custom alloys can be tested without atomization (Exp.)
- Only chemical composition is required for calculating shrinkage (Comp.)
- Computationally inexpensive (Comp.)

Disadvantages:

- Trade-off between measurable curvature and plastic deformation (Exp.)
- Local plasticity in the heat affected zone difficult to mitigate (Exp.)
- Best for high yield strength alloys (Exp.)
- No plasticity taken into account (Exp. & Comp.)
- So far the simulations work best for single phased alloys (Comp.)

**Author Contributions:** Conceptualization: A.A.; Funding acquisition: T.L.; Investigation: A.A., J.R. and J.L.; Methodology, A.A.; Project administration: T.L.; Software, A.A.; Supervision: M.L., T.P. and T.L.; Writing—original draft: A.A.; Writing—review editing: J.R., J.L., M.L., T.P. and T.L. All authors have read and agreed to the published version of the manuscript.

**Conflicts of Interest:** The authors declare no conflict of interest.

## Abbreviations

The following abbreviations are used in this manuscript:

| | |
|---|---|
| LPBF | Laser Powder Bed Fusion |
| AM | Additive Manufacturing |
| Finite Element Method | FEM |
| Direct energy deposition | DED |
| Linear coefficient of thermal expansion | CTE |
| Hexagonal close-packed | HCP |
| Body centered cubic | BCC |
| Face centered cubic | FCC |

## Appendix A. Plasticity Compensation of 316L with Comsol Multiphysics

The effect of plasticity was investigated with Comsol Multiphysics 6.0. The geometry was modeled using average dimensions of the five lasered 316L samples. Effect of top surface temperature on curvature was investigated by setting high temperatures starting from solidus and by cooling down to room temperature without heat dissipation in the base material. The assumption of no heat in base material is due to the waiting time in the experimental lasering setup and that no HAZ was visible in the base material. Ludwig plasticity model was used with hardening parameters *n* and *K*. Calculated with Equation (2), the residual stress value was very high at 3100 MPa. Best fit to experimental curvature was achieved when the top was cooled from 1490 K. This temperature represents the temperature above which stresses do not accumulate. Temperature dependent mechanical properties are shown in Figure A1. Residual stresses simulated with plasticity are shown in

the Table A1. Simulated curvature and residual stress distribution is shown in Figure A2 which is compared to experimental sample in Figure A3. Material properties for substrate properties were $\sigma_0$ = 200 MPa, $n$ = 0.4, $K$ = 1100 MPa, $E$ = 190 GPa. Thermal expansion coefficient was $19.9 \times 10^{-6}$ 1/K as calculated with Thermo-calc for the segregated system.
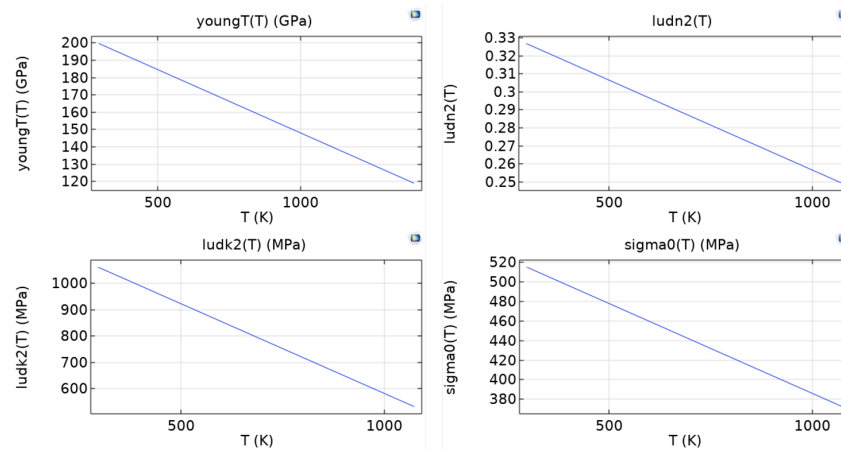


**Figure A1.** Temperature dependent hardening properties at strain rate of $1000\,\mathrm{s}^{-1}$ simplified from [49]. Young's modulus was taken from [50].
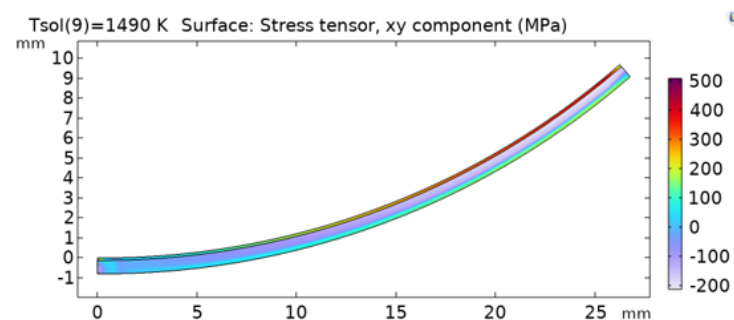


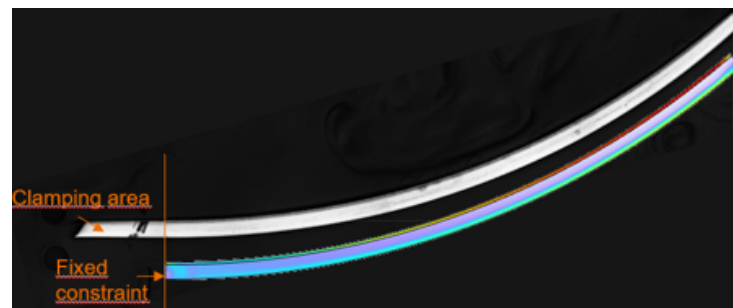**Figure A2.** Simulated curvature of lasered 316L sample.



**Figure A3.** Comparison of curvature between real (upper) and simulated (lower) samples.

**Table A1.** Stresses simulated with some plasticity.

| All Values in MPa | von Mises Stress | Stress Tensor, x Component | Stress Tensor, xy Component |
|---|---|---|---|
| Surface average Laser | 853.25 | 647.65 | 224.32 |
| Surface maximum Laser | 945.93 | 1065.8 | 508.26 |
| Surface average substrate | 281.94 | −117.2 | −40.924 |
| Surface maximum substrate | 559.67 | 463.63 | 185.26 |

As seen in Figure A3 the curvature in Comsol model is similar to the real sample and the calculated residual stresses (XY-component) are reasonable in Table A1. The sample tip

Y-direction displacement was measured to be 9.67 mm whereas the displacement in the Comsol model was 9.68 mm. The average von Mises stress in the lasered layer and the substrate are higher than yield strength, indicating the presence of plasticity that causes error when using Equation (2).

To analyse stress values correctly would require good temperature dependent material data, such as yield stress and hardening behavior, as well as elastic modulus. Additionally, the model should contain both heating and cooling because plasticity can take place in local heating as well. Usually, such data are not available during first stages of alloy development, and therefore plasticity compensation is not possible.

## Appendix B. TiCp with HCP+Liquid

In TiCp HCP+Liquid-system, liquid phase appears again at low temperatures giving proof that alpha prime martensite approximation in is not feasible for TiCp by disabling BCC from forming.
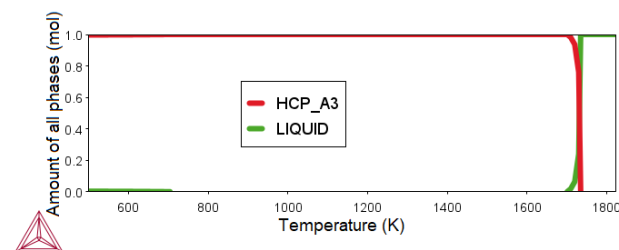


**Figure A4.** Phase fraction vs. temperature plot for TiCp system with HCP and liquid phases.

## Appendix C. Dendrite Radius

Figure A5 shows the microstructure of LPBD D2 tool steel with primary dendrite radius varying between 0.4–2 µm. The secondary dendrite radius is even smaller.
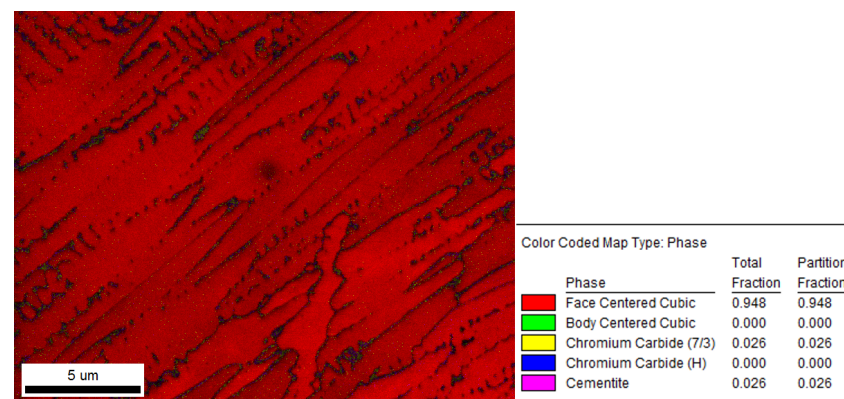


**Figure A5.** SEM image of the dendritic microstructure in LPBF D2 steel.

## References

1. Herzog, D.; Seyda, V.; Wycisk, E.; Emmelmann, C. Additive manufacturing of metals. *Acta Mater.* **2016**, *117*, 371–392. [CrossRef]
2. Salmi, A.; Atzeni, E.; Iuliano, L.; Galati, M. Experimental Analysis of Residual Stresses on AlSi10Mg Parts Produced by Means of Selective Laser Melting (SLM). *Procedia CIRP* **2017**, *62*, 458–463. [CrossRef]
3. DebRoy, T.; Wei, H.; Zuback, J.; Mukherjee, T.; Elmer, J.; Milewski, J.; Beese, A.; Wilson-Heid, A.; De, A.; Zhang, W. Additive manufacturing of metallic components—Process, structure and properties. *Prog. Mater. Sci.* **2018**, *92*, 112–224. [CrossRef]
4. Elsheikh, A.H.; Shanmugan, S.; Muthuramalingam, T.; Thakur, A.K.; Essa, F.A.; Ibrahim, A.M.M.; Mosleh, A.O. A comprehensive review on residual stresses in turning. *Adv. Manuf.* **2022**, *10*, 287–312. [CrossRef]
5. guang Chen, S.; jun Gao, H.; du Zhang, Y.; Wu, Q.; han Gao, Z.; Zhou, X. Review on residual stresses in metal additive manufacturing: Formation mechanisms, parameter dependencies, prediction and control approaches. *J. Mater. Res. Technol.* **2022**, *17*, 2950–2974. [CrossRef]

6. Pinomaa, T.; Yashchuk, I.; Lindroos, M.; Andersson, T.; Provatas, N.; Laukkanen, A. Process-Structure-Properties-Performance Modeling for Selective Laser Melting. *Metals* **2019**, *9*, 1138. [CrossRef]

7. Keller, T.; Lindwall, G.; Ghosh, S.; Ma, L.; Lane, B.M.; Zhang, F.; Kattner, U.R.; Lass, E.A.; Heigel, J.C.; Idell, Y.; et al. Application of finite element, phase-field, and CALPHAD-based methods to additive manufacturing of Ni-based superalloys. *Acta Mater.* **2017**, *139*, 244–253. [CrossRef]

8. Francois, M.; Sun, A.; King, W.; Henson, N.; Tourret, D.; Bronkhorst, C.; Carlson, N.; Newman, C.; Haut, T.; Bakosi, J.; et al. Modeling of additive manufacturing processes for metals: Challenges and opportunities. *Curr. Opin. Solid State Mater. Sci.* **2017**, *21*, 198–206. [CrossRef]

9. Ahmed, S.H.; Mian, A. Influence of Material Property Variation on Computationally Calculated Melt Pool Temperature during Laser Melting Process. *Metals* **2019**, *9*, 456. [CrossRef]

10. Fergani, O.; Berto, F.; Welo, T.; Liang, S.Y. Analytical modelling of residual stress in additive manufacturing. *Fatigue Fract. Eng. Mater. Struct.* **2017**, *40*, 971–978. [CrossRef]

11. Chadwick, A.F.; Voorhees, P.W. The development of grain structure during additive manufacturing. *Acta Mater.* **2021**, *211*, 116862. [CrossRef]

12. Zhang, C.; Yadav, V.; Moelans, N.; Juul Jensen, D.; Yu, T. The effect of voids on boundary migration during recrystallization in additive manufactured samples—A phase field study. *Scr. Mater.* **2022**, *214*, 114675. [CrossRef]

13. Yang, M.; Wang, L.; Yan, W. Phase-field modeling of grain evolution in additive manufacturing with addition of reinforcing particles. *Addit. Manuf.* **2021**, *47*, 102286. [CrossRef]

14. Lindroos, M.; Pinomaa, T.; Ammar, K.; Laukkanen, A.; Provatas, N.; Forest, S. Dislocation density in cellular rapid solidification using phase field modeling and crystal plasticity. *Int. J. Plast.* **2022**, *148*, 103139. [CrossRef]

15. Lindroos, M.; Pinomaa, T.; Antikainen, A.; Lagerbom, J.; Reijonen, J.; Lindroos, T.; Andersson, T.; Laukkanen, A. Micromechanical modeling approach to single track deformation, phase transformation and residual stress evolution during selective laser melting using crystal plasticity. *Addit. Manuf.* **2021**, *38*, 101819. [CrossRef]

16. Pinomaa, T.; Lindroos, M.; Walbrühl, M.; Provatas, N.; Laukkanen, A. The significance of spatial length scales and solute segregation in strengthening rapid solidification microstructures of 316L stainless steel. *Acta Mater.* **2020**, *184*, 1-16. [CrossRef]

17. Lukas, H.; Fries, S.G.; Sundman, B. *Computational Thermodynamics: The Calphad Method*; Cambridge University Press: Cambridge, UK, 2007. [CrossRef]

18. Gerstgrasser, M.; Cloots, M.; Stirnimann, J.; Wegener, K. Residual stress reduction of LPBF-processed CM247LC samples via multi laser beam strategies. *Int. J. Adv. Manuf. Technol.* **2021**, *117*, 2093–2103. [CrossRef]

19. Soffel, F.; Eisenbarth, D.; Wegener, K. Effect of clad height, substrate thickness and scanning pattern on cantilever distortion in direct metal deposition. *Int. J. Adv. Manuf. Technol.* **2021**, *117*, 2083–2091. [CrossRef]

20. Buchbinder, D.; Meiners, W.; Pirch, N.; Wissenbach, K.; Schrage, J. Investigation on reducing distortion by preheating during manufacture of aluminum components using selective laser melting. *J. Laser Appl.* **2014**, *26*, 012004. [CrossRef]

21. Wang, D.; Wu, S.; Yang, Y.; Dou, W.; Deng, S.; Wang, Z.; Li, S. The Effect of a Scanning Strategy on the Residual Stress of 316L Steel Parts Fabricated by Selective Laser Melting (SLM). *Materials* **2018**, *11*, 1821. [CrossRef]

22. Wu, A.S.; Brown, D.W.; Kumar, M.; Gallegos, G.; King, W.E. An Experimental Investigation into Additive Manufacturing Induced Residual Stresses in 316L Stainless Steel. *Metall. Mater. Trans.* **2014**, *45*, 6260–6270. [CrossRef]

23. Prabhakar, P.; Sames, W.; Dehoff, R.; Babu, S. Computational modeling of residual stress formation during the electron beam melting process for Inconel 718. *Addit. Manuf.* **2015**, *7*, 83–91. [CrossRef]

24. Denlinger, E.R.; Heigel, J.C.; Michaleris, P.; Palmer, T. Effect of inter-layer dwell time on distortion and residual stress in additive manufacturing of titanium and nickel alloys. *J. Mater. Process. Technol.* **2015**, *215*, 123–131. [CrossRef]

25. Mertens, R.; Vrancken, B.; Holmstock, N.; Kinds, Y.; Kruth, J.P.; Van Humbeeck, J. Influence of Powder Bed Preheating on Microstructure and Mechanical Properties of H13 Tool Steel SLM Parts. *Phys. Procedia* **2016**, *83*, 882–890. [CrossRef]

26. Macherauch, E. Introduction to Residual Stress. In *Residual Stresses*; Niku-Lari, A., Ed.; Pergamon Press: Cambridge, UK, 1987; pp. 1–36. [CrossRef]

27. Bartlett, J.L.; Li, X. An overview of residual stresses in metal powder bed fusion. *Addit. Manuf.* **2019**, *27*, 131–149. [CrossRef]

28. Stoney, G. The Tension of Metallic Films Deposited by Electrolysis. *Proc. R. Soc. Math. Phys. Eng. Sci.* **1909**, *82*, 172–175. [CrossRef]

29. Brenner, A.; Senderoff, S. Calculation of stress in electrodeposits from the curvature of a plated strip. *J. Res. Natl. Bur. Stand.* **1949**, *42*, 105. [CrossRef]

30. Ohring, M. *Materials Science of Thin Films*; Elsevier Science Technology: London, UK, 2001.

31. Suhonen, T.; Varis, T.; Dosta, S.; Torrell, M.; Guilemany, J. Residual stress development in cold sprayed Al, Cu and Ti coatings. *Acta Mater.* **2013**, *61*, 6329–6337. [CrossRef]

32. Simson, T.; Emmel, A.; Dwars, A.; Böhm, J. Residual stress measurements on AISI 316L samples manufactured by selective laser melting. *Addit. Manuf.* **2017**, *17*, 183–189. [CrossRef]

33. Qiu, C.; Kindi, M.A.; Aladawi, A.S.; Hatmi, I.A. A comprehensive study on microstructure and tensile behaviour of a selectively laser melted stainless steel. *Sci. Rep.* **2018**, *8*, 7785. [CrossRef]

34. Saarimäki, J.; Lundberg, M.; Moverare, J.; Brodin, H. 3D Residual Stresses in Selective Laser Melted Hastelloy X. *Mater. Res. Proc.* **2017**, *2*, 73–78. [CrossRef]

35. Reijonen, J.; Antikainen, A.; Lagerbom, J.; Lindroos, M.; Pinomaa, T.; Lindroos, T. Laser powder bed fusion of high carbon tool steels. In Proceedings of the World PM2022 Congress Proceedings, Lyon, France, 9–13 October 2022.

36. Lu, X.G.; Selleby, M.; Sundman, B. Theoretical modeling of molar volume and thermal expansion. *Acta Mater.* **2005**, *53*, 2259–2272. [CrossRef]

37. MatWeb LLC. AISI Type 316L Stainless Steel, Annealed Sheet. Available online: https://www.matweb.com/search/DataSheet.aspx?MatGUID=1336be6d0c594b55afb5ca8bf1f3e042 (accessed on 20 June 2022).

38. Antikainen, A.; Reijonen, J.; Lagerbom, J.; Lindroos, T. (VTT Technical Research Centre of Finland, Tampere, Finland). Additive manufacturing and heat treatment of high carbon cold work tool steel D2. Unpublished work, 2022.

39. MatWeb LLC. Titanium Ti-6Al-4V (Grade 5), Annealed. Available online: https://www.matweb.com/search/DataSheet.aspx?MatGUID=a0655d261898456b958e5f825ae85390 (accessed on 20 June 2022).

40. Electro Optical Systems GmBH. *EOS Titanium Ti64 M290 Material Datasheet*. CR326 11-17.

41. MatWeb LLC. Titanium Grade 2. Available online: https://www.matweb.com/search/DataSheet.aspx?MatGUID=24293fd5831941ec9fa01dce994973c7 (accessed on 20 June 2022).

42. Electro Optical Systems GmBH. *EOS Titanium TiCp Grade 2 for M290 Material Datasheet*. CR284 v01, 30 May 2016.

43. MatWeb LLC. Special Metals INCONEL® HX Nickel Superalloy (UNS N06002). Available online: https://www.matweb.com/search/DataSheet.aspx?MatGUID=1fa55846a31c42119e5abd12fde717b8 (accessed on 20 June 2022).

44. Electro Optical Systems GmBH. *EOS Nickel Alloy HX for M290 Material Datasheet*. TMS/0.2015.

45. Mercelis, P.; Kruth, J. Residual stresses in selective laser sintering and selective laser melting. *Rapid Prototyp. J.* **2006**, *12*, 254–265. [CrossRef]

46. Yin, Y.; Zhang, J.; Gao, J.; Zhang, Z.; Han, Q.; Zan, Z. Laser powder bed fusion of Ni-based Hastelloy X superalloy: Microstructure, anisotropic mechanical properties and strengthening mechanisms. *Mater. Sci. Eng.* **2021**, *827*, 142076. [CrossRef]

47. Casati, R.; Lemke, J.; Vedani, M. Microstructure and Fracture Behavior of 316L Austenitic Stainless Steel Produced by Selective Laser Melting. *J. Mater. Sci. Technol.* **2016**, *32*, 738–744. [CrossRef]

48. Antikainen, A.; Reijonen, J.; Lagerbom, J.; Lindroos, M.; Pinomaa, T.; Lindroos, T. Single-Track Laser Scanning as a Method for Evaluating Printability: The Effect of Substrate Heat Treatment on Melt Pool Geometry and Cracking in Medium Carbon Tool Steel. *J. Mater. Eng. Perform.* **2022**, [CrossRef]

49. Lee, W.S.; Chen, T.H.; Lin, C.F.; Luo, W.Z. Dynamic Mechanical Response of Biomedical 316L Stainless Steel as Function of Strain Rate and Temperature. *Bioinorg. Chem. Appl.* **2011**, *2011*, 173782. [CrossRef] [PubMed]

50. British Stainless Steel Association. Elevated Temperature Physical Properties of Stainless Steels. Available online: https://bssa.org.uk/bssa_articles/elevated-temperature-physical-properties-of-stainless-steels/ (accessed on 7 July 2022).